

Exploiting voxel-sparsity for bone imaging with sparse-view cone-beam computed tomography

Emil Y. Sidky^a, Holly L. Stewart^b, Christopher E. Kawcak^b, C. Wayne McIlwraith^b, Martine C. Duff^c, Xiaochuan Pan^a

^a The University of Chicago, Department of Radiology MC-2026, 5841 S. Maryland Avenue, Chicago IL, 60637

^b Colorado State University, Department of Clinical Sciences, College of Veterinary Medicine and Biomedical Sciences, Fort Collins, CO, 80523

^c Savannah River National Laboratory, Aiken, SC, 29808

Abstract. An optimization-based image reconstruction framework is developed specifically for bone imaging. This framework exploits voxel-sparsity by use of ℓ_1 -norm image regularization and it enables image reconstruction from sparse-view cone-beam computed tomography (CBCT) acquisition. The effectiveness of the voxel-sparsity regularization is enhanced by using a blurred image representation. Ramp-filtering is included in the data discrepancy term and it has the effect of acting as a preconditioner, reducing the necessary number of iterations. The bone image reconstruction framework is demonstrated on CBCT data taken from an equine metacarpal condyle specimen.

1 Introduction

The majority of sparsity-exploiting image reconstruction techniques for sparse-view cone-beam computed tomography (CBCT) have employed total-variation (TV) as a sparsity regularizer because gradient sparsity is an effective prior for X-ray based imaging.^{1,2} Prior to this work, it was suggested that voxel-sparsity itself could be useful for application with few-view CBCT for imaging sparse structures such as blood vessel trees in CT angiography.³ When applying sparsity-regularization to bone imaging, deciding between gradient and voxel sparsity is not obvious. Bone tissue occupies more volume than truly sparse structures such as blood vessels but less volume than the soft tissue. Bones also have high-contrast fine trabecular structure. Porosity will increase the number of non-zeros in a gradient-magnitude image but it will improve voxel sparsity, thus favoring the latter. Further complicating this decision is that some of the fine bone structures may not be resolvable by the CBCT system. Even though the underlying bone tissue may be porous on a scale of ≈ 10 microns or less, it will appear uniform at standard CBCT resolution, ≈ 200 microns, thus favoring the use of gradient sparsity.

In a prior study, we employed a micro-CT scan of an equine limb sample to generate a high-resolution computer phantom for studying sparsity regularization for image reconstruction in sparse-view CBCT.⁴ In that work it was found that use of voxel sparsity regularization was more effective at reducing the streaks due to view-angle undersampling in CBCT. A model was developed that expresses the reconstructed volume in terms of a blurred voxel-sparse image.

In this work, we apply this model to an actual CBCT scan of a horse limb sample. A full 720-view CBCT dataset is collected and sparse-view configurations are generated by sub-sampling this dataset. In Sec. 2, we review the optimization-based model used for image reconstruction in sparse-view CBCT of bone tissue. In Sec. 3, reconstruction slice images are shown demonstrating the parameter dependences of the algorithm. We conclude this abstract in Sec. 4.

2 The optimization-based framework for CBCT bone imaging

The proposed CBCT bone image reconstruction framework is based on the following optimization problem

$$\min_f \frac{1}{2} (XB_w f - g)^\top R (XB_w f - g) \text{ such that } \|f\|_1 \leq \gamma, \quad (1)$$

where the CBCT data and image volume are represented by an m -dimensional vector g and n -dimensional vector f , respectively; the $m \times n$ matrix X denotes CBCT projection; the $n \times n$ matrix B_w is Gaussian blurring using a width parameter w ; the $m \times m$ matrix R is block-diagonal, where each block performs ramp filtering on each projection view; and γ is the constraint parameter on the volume image ℓ_1 -norm. The ramp filter R has two purposes: (1) it accelerates convergence as demonstrated in Ref.,⁵ and (2) it can reduce artifacts due to low-frequency inconsistencies in the projection in a manner similar to the approach in Ref.⁶ The actual reconstructed volume is represented by $B_w f$ and voxel sparsity is enforced on the underlying image f ; in this way images with smooth transitions between tissue types can be represented with a high-degree of voxel sparsity.⁷



Fig 1 FBP reconstructed slice images from the full CBCT dataset consisting of 720 views. The shown slices are for orthogonal planes that intersect at the lucency indicated by the red arrows. The image on the right corresponds to a trans-axial slice. The grayscale window is $[0.02, 0.32] \text{ cm}^{-1}$.

To solve Eq. (1), we employ the primal-dual (PD) algorithm developed by Chambolle and Pock.^{8,9} To facilitate our PD implementation, we absorb the filtering operation into a combined system matrix and Eq. (1) is modified to

$$\min_f \frac{1}{2} \|M_w f - Sg\|_2^2 \text{ such that } \|f\|_1 \leq \gamma,$$

where

$$M_w = SXB_w, \text{ and } R = S^2.$$

The matrix S is the square root of the the ramp filter matrix, which can be computed readily in the frequency domain where the ramp filtering matrix is diagonal. The resulting algorithm has three control parameters: the iteration number, the ℓ_1 -norm constraint parameter γ , and the voxel blur width w . We demonstrate the impact of all of these parameters on image reconstruction from sparse-view CBCT data of an equine limb specimen.

3 Results

We apply the bone image reconstruction algorithm to a CBCT data set acquired on an Epica Pegaso veterinary CT scanner. Three sparse-view configurations are investigated with a short-scan arc of 192 degrees; we consider 128, 64, and 32 views evenly spaced over the short-scan arc which corresponds to an angular spacing of 1.5, 3, and 6 degrees, respectively. All of the sparse-view CBCT datasets are subsampled from a full 720-view circular scan, and accordingly the modeled exposure decreases with the projection view number. The detector size is 1088x896 detector pixels, where each pixel is $(0.278\text{mm})^2$ in size. Image volumes are reconstructed onto a $768 \times 768 \times 512$ voxel grid using cubic voxels with a width of 0.2085 mm. A reference volume is reconstructed by use of filtered back-projection (FBP) applied to the full 720-view dataset and shown in Fig. 1. The red arrows in the figure demonstrate subchondral bone lysis typical of a palmar osteochondral lesion in racehorses that are of clinical significance.

Varying the iteration number

In the first set of results for using the bone sparsity image reconstruction algorithm, we subsample the full 720-view dataset to a 64-view dataset over a 192 degree scanning arc. Setting $w = 1$ and $\gamma = 5.0 \times 10^6$, slice images of the reconstructed volume are shown at 10, 20, and 50 iterations in Fig. 2. Through this progression of images, there is a clear trend of improving spatial resolution with iteration number up to the 50th iteration. Beyond this, the volume iterates change very little as demonstrated by the fact that there is little difference between the images at 50 and 100 iterations. For the remainder of the results shown in this abstract, we set the iteration number to 50.

In comparing the bottom row of images, at 50 iterations, to the FBP reference in Fig. 1 there is a noticeable loss in image quality, as might be expected since the view number is reduced by more than a factor of 10; however, features of clinical interest, such as the lucency in the bone tissue, are still clearly visible.

Varying the volume ℓ_1 -norm constraint parameter γ

In the second parametric study, we investigate the impact of varying γ . Using the 64-view dataset, and setting the iteration number to 50 and $w = 0.2085$ mm, Fig. 3 shows reconstructed slice images for four values of γ , decreasing from top to bottom. The maximum value of $\gamma = 8.0 \times 10^6$ is chosen because at this value the ℓ_1 -norm constraint

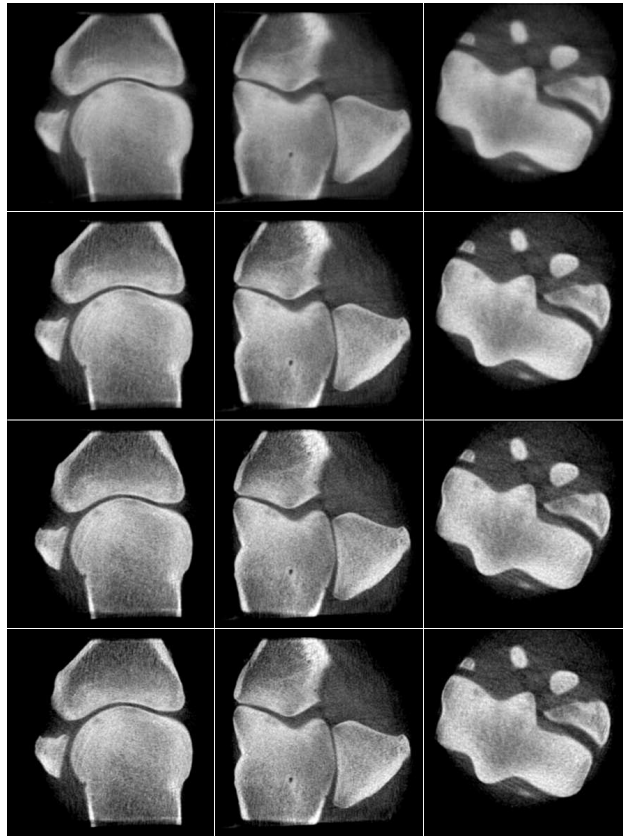


Fig 2 Progression of the volume images with iteration number for reconstruction from a 64-view dataset spanning a 192 degree arc. The algorithm settings are $\gamma = 5.0 \times 10^6$, $0.0166 \text{ cm}^{-1}/\text{voxel}$, and $w = 0.2085 \text{ mm}$, 1 voxel width. The shown slice images correspond to the same slices in Fig. 1. The rows correspond to the reconstructed volume at iteration 10 (1st row), 20 (2nd row), 50 (3rd row), and 100 (4th row). The grayscale window is $[0.02, 0.32] \text{ cm}^{-1}$.

is just barely active; with no ℓ_1 -norm constraint the PD iterations achieves a volume with an ℓ_1 -norm of 8.17×10^6 . As by design, the images become more voxel sparse as γ decreases; at the largest value of γ , all of the soft-tissue is visible along with artifacts outside of the support of the sample. As γ decreases the non-zero voxel values outside of the object support begin to disappear. Driving to lower γ , the voxel values all decrease in magnitude and the soft tissue voxels also begin to disappear. At the lowest shown value of γ , only voxels containing bone tissue remain albeit at a reduced amplitude compared with the FBP reference of Fig. 1.

A less intuitive result of tightening the ℓ_1 -norm constraint on the volume, i.e. reducing γ , is that the image resolution appears to improve as γ decreases. This trend runs counter to most other forms of regularization, where increasing the regularization strength tends to decrease spatial resolution. The marked increase in spatial resolution with reduced γ is a direct result of enforcing voxel sparsity on high-contrast porous bone tissue. Furthermore, ℓ_1 regularization does not penalize the difference between neighboring voxels, as many regularizers do. The apparent spatial resolution of the bone tissue improves mainly in going from $\gamma = 8.0 \times 10^6$ to $\gamma = 6.0 \times 10^6$. Decreasing γ further mainly impacts the bone tissue gray level. For the final set of results, this constraint is set to $\gamma = 5.0 \times 10^6$, a value that does not compromise spatial resolution and yet does not eliminate voxels at or near the bone tissue.

Varying w and scan configuration

For the final set of results, we consider three scan configurations using the 192 degree scanning arc with different angular sampling intervals as dictated by selecting 128, 64, and 32 evenly space projection view angles and shown in Figs. 4, 5, and 6, respectively. For each scan configuration image reconstruction is performed for w set to 0.417

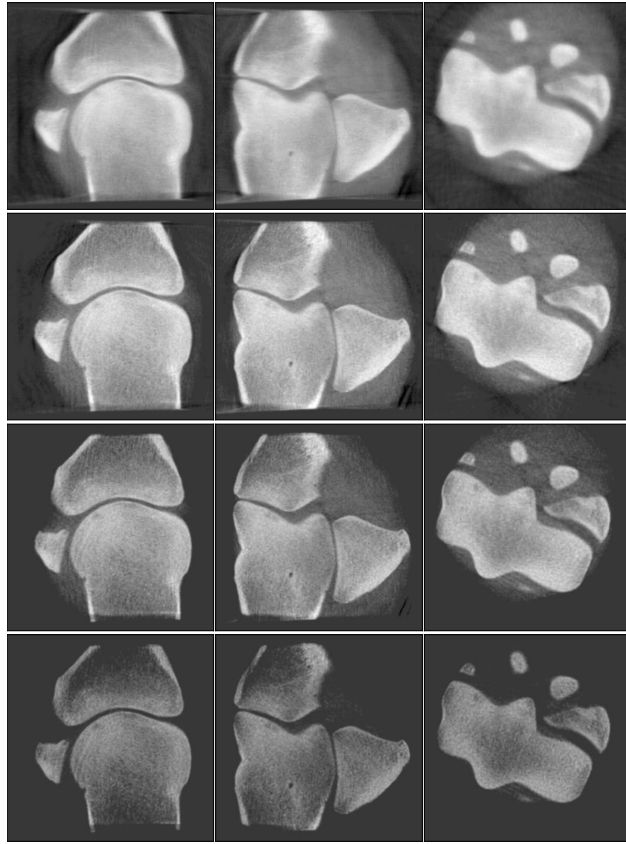


Fig 3 Impact of varying γ on the volume images for image reconstruction from a 64-view dataset spanning a 192 degree arc. The other algorithm parameters, the iteration number and blur kernel width, are set to 50 iterations and $w = 0.2085$ mm, 1 voxel width, respectively. The γ constraint values are set to 8.0×10^6 (1st row), 6.0×10^6 (2nd row), 4.0×10^6 (3rd row), and 2.0×10^6 (4th row). The grayscale window is set wider, at $[-0.1, 0.35] \text{ cm}^{-1}$, than that of the other figures in order to appreciate the numbers of non-zero voxels.

mm (two voxel widths), 0.2085 mm (one voxel width) and zero mm for fixed iteration number and γ . We combine the w -dependence together with the display of images from different scan configurations, because the w -parameter is intended as the main control parameter on the image quality. For all configurations increasing w yields smoother images for the resulting reconstructed volume. Fine-tuning w will depend on the desired image quality metric that should be optimized. For the present discussion, we focus on $w = 1.0$, the middle row of these figures.

The 128-view scan results shown in Fig. 4 have decent image quality for the bone tissue with minimal streak artifacts and reasonably high spatial resolution. The lucent bone defect is still clearly visible in the $w = 1$ series of images. This scan also represents a six-fold reduction in the number of projections from the original CBCT dataset. Shown in Fig. 5 are the resulting images for a 64-view scan, a twelve-fold reduction in the number of views. The resolution is somewhat degraded in comparison with the 128-view results and mild streak artifacts overlapping the bone tissue become apparent, although the bone lucency is still visible. In the final set of results in Fig. 6, the view sampling is reduced by another factor of two, and the dataset contains only 32 views. For these images, the streak artifacts begin to seriously degrade the image quality and spatial resolution is markedly worse than the results for the 64-view configuration. Even so, some bone features are still visible and there may be clinical utility for this scan configuration.

4 Conclusion

We have demonstrated an optimization-based framework for sparse-view CBCT image reconstruction designed for bone imaging using real CBCT data taken of an equine limb sample. The model involves representing the image as a

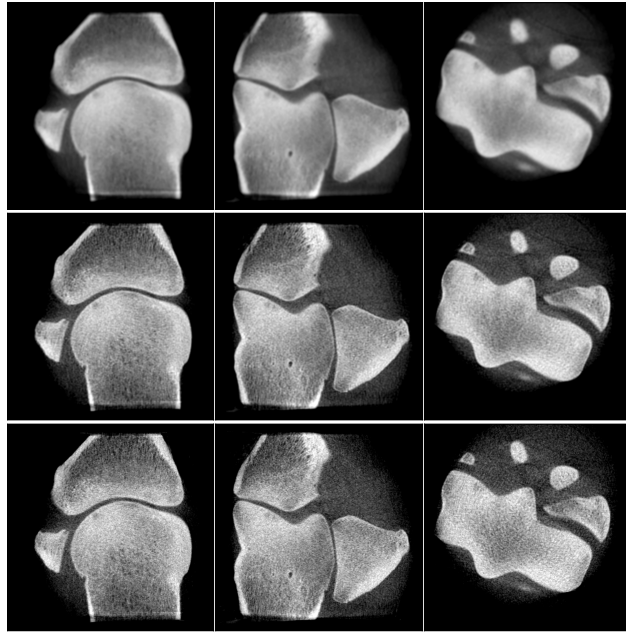


Fig 4 Slice images of reconstructed volumes from the 128-view dataset using $w = 2 \times 0.2085$ mm (Top row) $w = 0.2085$ mm (Middle row), and $w = 0.0$ mm (Bottom row) at 50 iterations and $\gamma = 5.0 \times 10^6$. The grayscale window is $[0.02, 0.32] \text{ cm}^{-1}$.

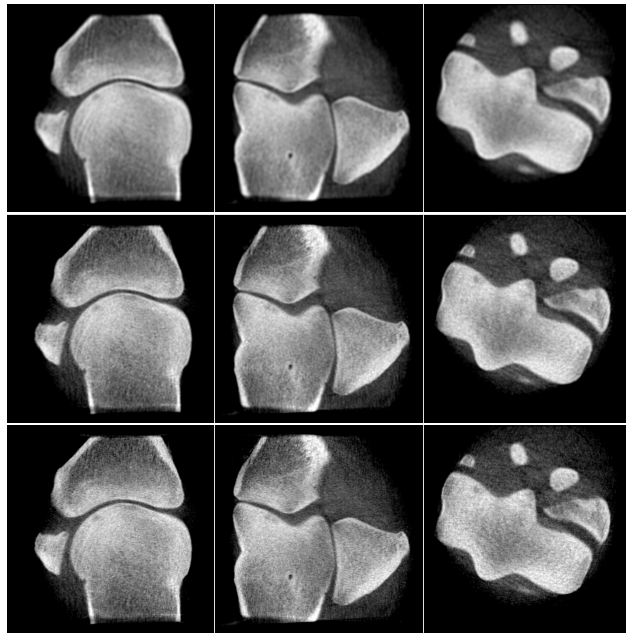


Fig 5 Slice images of reconstructed volumes from the 64-view dataset using $w = 2 \times 0.2085$ mm (Top row) $w = 0.2085$ mm (Middle row), and $w = 0.0$ mm (Bottom row) at 50 iterations and $\gamma = 5.0 \times 10^6$. The grayscale window is $[0.02, 0.32] \text{ cm}^{-1}$.

blurred voxel-sparse image. The use of an ℓ_1 -norm constraint on the reconstructed volume encourages voxel sparsity, which is useful for bone image because bone tissue takes up less volume than the surrounding soft tissue and it can have porous trabecular structure that is resolvable by the CBCT system. No explicit roughness regularizations is used in the framework other than the regularization that is afforded by the blurring kernel of the object model. Additional roughness regularization may not be necessary due to the high contrast of bone tissue in X-ray imaging. The results of

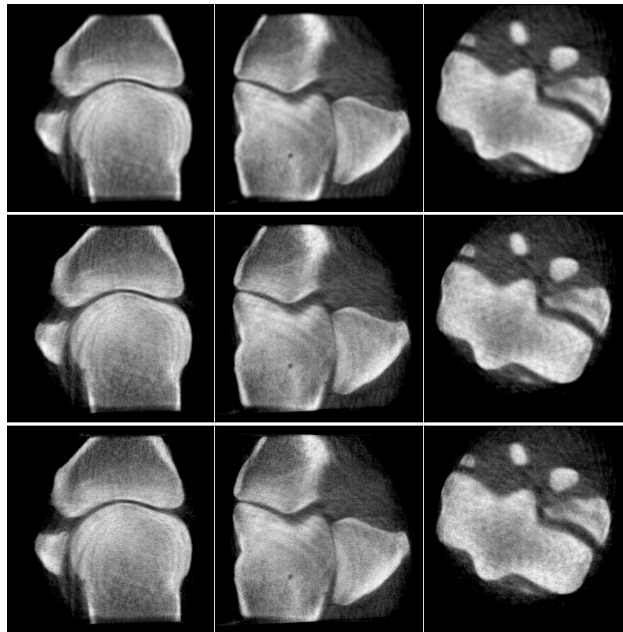


Fig 6 Slice images of reconstructed volumes from the 32-view dataset using $w = 2 \times 0.2085$ mm (Top row) $w = 0.2085$ mm (Middle row), and $w = 0.0$ mm (Bottom row) at 50 iterations and $\gamma = 5.0 \times 10^6$. The grayscale window is $[0.02, 0.32] \text{ cm}^{-1}$.

applying the proposed bone imaging framework to sparse-view data show that greatly reduced view-angle sampling has the potential to yield clinically useful images and possibly enable new CBCT scan configurations for equine limb imaging. The development of new scan configurations may provide an opportunity to develop screening techniques useful to injury prevention in horses, potentially translating into other species.

Acknowledgment

This work was supported in part by the Grayson-Jockey Club Research Foundation and NIH Grant Nos. R01-EB026282 and R01-EB023968. MCD is also supported by Savannah River National Laboratory, which is operated by Battelle Savannah River Alliance for the U.S. Department of Energy under Contract No. 89303321CEM000080. The contents of this article are solely the responsibility of the authors and do not necessarily represent the official views of the National Institutes of Health.

References

- 1 E. J. Candès, J. Romberg, and T. Tao, "Robust uncertainty principles: Exact signal reconstruction from highly incomplete frequency information," *IEEE Transactions on information theory* **52**(2), 489–509 (2006).
- 2 E. Y. Sidky and X. Pan, "Image reconstruction in circular cone-beam computed tomography by constrained, total-variation minimization," *Phys. Med. Biol.* **53**, 4777 (2008).
- 3 M. Li, H. Yang, and H. Kudo, "An accurate iterative reconstruction algorithm for sparse objects: application to 3D blood vessel reconstruction from a limited number of projections," *Phys. Med. Biol.* **47**, 2599–2609 (2002).
- 4 E. Y. Sidky, H. L. Stewart, C. E. Kawcak, *et al.*, "Bone sparsity model for computed tomography image reconstruction," in *15th International Meeting on Fully Three-Dimensional Image Reconstruction in Radiology and Nuclear Medicine*, **11072**, 110721U (2019).
- 5 T. Wang, H. Kudo, F. Yamazaki, *et al.*, "A fast regularized iterative algorithm for fan-beam CT reconstruction," *Phys. Med. Biol.* **64**, 145006 (2019).
- 6 E. Y. Sidky, D. N. Kraemer, E. G. Roth, *et al.*, "Analysis of iterative region-of-interest image reconstruction for x-ray computed tomography," *J. Med. Imag.* **1**, 031007 (2014).

- 7 P. A. Wolf, J. S. Jørgensen, T. G. Schmidt, *et al.*, “Few-view single photon emission computed tomography (SPECT) reconstruction based on a blurred piecewise constant object model,” *Phys. Med. Biol.* **58**, 5629–5652 (2013).
- 8 A. Chambolle and T. Pock, “A first-order primal-dual algorithm for convex problems with applications to imaging,” *J. Math. Imag. Vis.* **40**, 120–145 (2011).
- 9 E. Y. Sidky, J. H. Jørgensen, and X. Pan, “Convex optimization problem prototyping for image reconstruction in computed tomography with the Chambolle–Pock algorithm,” *Phys. Med. Biol.* **57**, 3065–3091 (2012).